The Astrophysical Journal, 913:46 (10pp), 2021 May 20 https://doi.org/10.3847/1538-4357/abf354

Competitive Dehydrogenation and Backbone Fragmentation of Superhydrogenated PAHs: A Laboratory Study

Mark H. Stockett[1], Lorenzo Avaldi[2], Paola Bolognesi[2], James N. Bull[3], Laura Carlini[2], Eduardo Carrascosa[4], Jacopo Chiarinelli[2], Robert Richter[5], and Henning Zettergren[1]
[1] Fysikum, Stockholms Universitet, Stockholm, Sweden; Mark.Stockett@fysik.su.se
[2] CNR-Istituto di Struttura della Materia, Area della Ricerca di Roma 1, Rome, Italy
[3] School of Chemistry, University of East Anglia, Norwich, UK
[4] Laboratoire de Chimie Physique Moléculaire, École Polytechnique Fédérale de Lausanne, Lausanne, Switzerland
[5] Elettra Sincrotrone Trieste, Trieste, Italy
Received 2020 November 27; revised 2021 March 6; accepted 2021 March 28; published 2021 May 24

Abstract

Superhydrogenated polycyclic aromatic hydrocarbons (PAHs) have been suggested to catalyze the formation of H_2 in certain regions of space, but it remains unclear under which circumstances this mechanism is viable given the reduced carbon backbone stability of superhydrogenated PAHs. We report a laboratory study on the stability of the smallest pericondensed PAH, pyrene ($C_{16}H_{10+N}$, with $N = 4$, 6, and 16 additional H atoms), against photodestruction by single vacuum ultraviolet photons using the photoelectron–photoion coincidence technique. For $N = 4$, we observe a protective effect of hydrogenation against the loss of native hydrogens, in the form of an increase in the appearance energies of the $C_{16}H_9^+$ and $C_{16}H_8^+$ daughter ions compared to those reported for pristine pyrene ($C_{16}H_{10}$). No such effect is seen for $N = 6$ or 16, where the weakening effect of replacing aromatic bonds with aliphatic ones outweighs the buffering effect of the additional hydrogen atoms. The onset of fragmentation occurs at similar internal energies for $N = 4$ and 6, but is significantly lower for $N = 16$. In all three cases, H-loss and C_mH_n-loss ($m \geqslant 1$, carbon backbone fragmentation) channels open at approximately the same energy. The branching fractions of the primary channels favor H-loss for $N = 4$, C_mH_n-loss for $N = 16$, and are roughly equal for the intermediate $N = 6$. We conclude that superhydrogenated pyrene is probably too small to support catalytic H_2-formation, while trends in the current and previously reported data suggest that larger PAHs may serve as catalysts up to a certain level of hydrogenation.

Unified Astronomy Thesaurus concepts: Polycyclic aromatic hydrocarbons (1280); Astrochemistry (75); Laboratory astrophysics (2004); Photodissociation regions (1223); Reaction catalysts (2080)

1. Introduction

Molecular hydrogen is the most abundant molecule in the universe and the key ingredient for star formation (Tielens 2005). It has been proposed that, under certain circumstances, polycyclic aromatic hydrocarbons (PAHs) may play a catalytic role in H_2 formation (Bauschlicher 1998; Hirama et al. 2004; Castellanos et al. 2018a). This may be particularly important in regions that are too warm (>20 K) for the otherwise successful model, association of H atoms on the surface of dust grains (Hollenbach & Salpeter 1971), to operate efficiently. For example, inexplicably high H_2-formation rates have been inferred for photodissociation regions (PDRs) with elevated PAH abundances (Habart et al. 2003, 2004). Superhydrogenated PAHs (HPAHs), which contain extra H atoms in addition to the native ones present in pristine PAHs, may play an important role in molecular hydrogen formation in these regions (Mennella et al. 2012; Ferullo et al. 2019). While not definitively identified in space, laboratory (Wagner et al. 2000; Sandford et al. 2013) and computational (Pauzat & Ellinger 2001; Mackie et al. 2018) studies have suggested that HPAHs may contribute to the so-called aromatic infrared bands (Tielens 2008) at wavelengths between 3.4 and 3.6 μm. Highly hydrogenated PAHs have been shown to be readily formed under a variety of circumstances (Boschman et al. 2012; Thrower et al. 2012, 2014; Klærke et al. 2013; Cazaux et al. 2016; Cruz-Diaz et al. 2020; Schlathölter et al. 2020), and efficient photoinduced H_2 formation from HPAHs has been demonstrated (Vala et al. 2009; Szczepanski et al. 2010; Fu et al. 2011; Foley et al. 2018).

The formation, destruction, and properties of HPAHs are topical subjects within laboratory astrophysics. A central question is the stability of HPAHs under the conditions prevailing in space. The binding of additional H atoms to PAHs replaces aromatic sp^2 bonds with aliphatic sp^3 bonds, weakening the carbon backbone. On the other hand, the additional H atoms may act as a buffer against dissociation. This was demonstrated in experiments where superhydrogenated coronene ($C_{24}H_{12+N}$, $N = 1$, 3, 5) cations were found to lose fewer of their native H atoms with increasing levels of superhydrogenation following soft X-ray excitation at 285 eV (Reitsma et al. 2014). More recent studies, however, showed that higher degrees of superhydrogenation ($N \gtrsim 6$) led to increased carbon backbone fragmentation (Rapacioli et al. 2018; Cazaux et al. 2019). Taken together, these studies suggest the existence of a window of hydrogenation levels consistent with truly catalytic H_2-formation without destruction of the native PAH. The challenge is to constrain the width of this window for a range of PAH sizes to ascertain under which astronomical conditions this process may be relevant.

In this article, we present a laboratory study of superhydrogenated pyrene $C_{16}H_{10+N}$, where $N = 4$, 6, and 16 additional hydrogen atoms. The structures of these molecules are presented in Figure 1. Previous investigations of this model system have shown that hydrogenation leads both to larger fragmentation cross sections (Gatchell et al. 2015) and lower

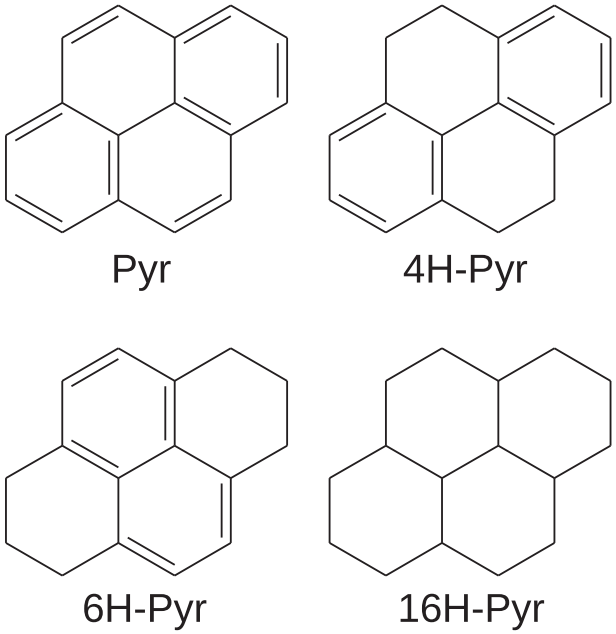

Figure 1. Pristine pyrene (Pyr, $C_{16}H_{10}$), tetrahydropyrene (4H-Pyr, $C_{16}H_{14}$), hexahydropyrene (6H-Pyr, $C_{16}H_{16}$), and hexadecahydropyrene (16H-Pyr, $C_{16}H_{26}$).

threshold energies for destruction in collisions with atoms (Stockett et al. 2015; Wolf et al. 2016a). Such collisions with H, He, and C atoms are thought to be an important destruction mechanism for PAHs in supernova shocks (Micelotta et al. 2010; Postma et al. 2010). It was further shown that less energy was required to induce fragmentation of the carbon backbone for hydrogenated pyrene than pristine pyrene in multiphoton dissociation mass spectrometry experiments (Wolf et al. 2016b). Here, we utilize the Photo-Electron Photo-Ion Coincidence (PEPICO) technique to elucidate the lowest-energy dissociation pathways of superhydrogenated pyrene upon the absorption of single vacuum ultraviolet (VUV) photons. This is perhaps the most relevant form of activation for comparison to astrochemical models, where heating by single VUV photons is supposed to induce dissociation of PAHs in competition with vibrational infrared emission (Allamandola et al. 1989). While both pyrene and coronene are smaller than the PAH molecules thought to be abundant in PDRs, they incorporate the essential chemical groups relevant to H_2-formation.

Pristine pyrene ($C_{16}H_{10}$), the smallest pericondensed PAH, has been the subject of several VUV-photodissociation experiments (Ling et al. 1995; Jochims et al. 1999; West et al. 2014c; Rouillé et al. 2015) and closely related photoelectron spectroscopy studies (Mayer et al. 2011; Mishra et al. 2014). Of special interest is the competition between the loss of molecular hydrogen and the sequential loss of hydrogen atoms. H_2-loss is energetically favored but sequential 2H-loss is entropically favored, with H_2-emission becoming significant only at high excitation energies (Chen et al. 2015). Pyrene molecules with various substitutions have also been recently investigated (Rouillé et al. 2015; West et al. 2018), as have a few smaller HPAHs (Mayer et al. 2011; West et al. 2014a; Diedhiou et al. 2019).

Very recently, Diedhiou et al. (2020) investigated the photostability of superhydrogenated catacondensed PAHs anthracene and phenanthrene in a PEPICO experiment where threshold electrons are detected. Compared to the same group's earlier study of pristine anthracene (West et al. 2014b), they observe a weak protective effect for dihydroanthracene in the form of an increased relative yield of the H-loss dissociation channel versus the main backbone fragmentation channel. For higher degrees of hydrogenation, backbone fragmentation dominates. The present study bridges the gap between the work of Diedhiou et al. (2020), as well as that of the Groningen group on coronene (Reitsma et al. 2014; Foley et al. 2018; Rapacioli et al. 2018), by considering the intermediate size, pericondensed pyrene system.

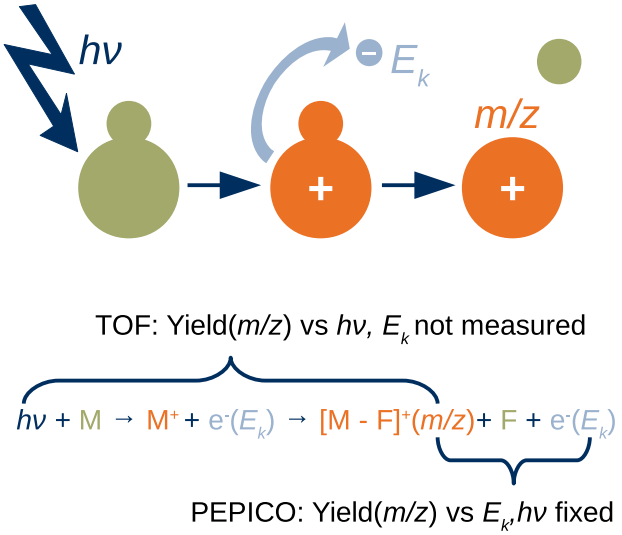

Figure 2. Comparison of the measurement principles of PEPICO and TOF methods, where $h\nu$ is the incoming photon energy, E_k is the electron kinetic energy, and m/z is the mass-to-charge ratio of the daughter ion.

2. Experimental Methods

Experiments were performed at the CiPO beamline (Derossi et al. 1995) of the Elettra synchrotron using an endstation designed for electron-ion coincidence experiments. The experimental setup (Plekan et al. 2008) and procedures (Chiarinelli et al. 2018) have been described previously. Briefly, the endstation is equipped with a commercial 150 mm mean radius hemispherical electron energy analyzer (VG 220i) mounted at the magic angle with respect to the incident linearly polarized radiation and a time-of-flight mass spectrometer mounted opposite to the electron analyzer. The two analyzers can be operated independently, for photoelectron spectroscopy (PES) and time-of-flight mass spectrometry (TOF-MS), or in time coincidence for photoelectron–photoion coincidence (PEPICO) experiments. An illustration of the latter two methods is given in Figure 2. Recently, the hemispherical analyzer has been equipped with a position-sensitive detector (Cautero et al. 2008; Menk et al. 2019) that replaced the original detection system made of six independent channeltrons (Plekan et al. 2008), leading to a significant improvement in terms of efficiency and resolution.

The PEPICO measurements were performed at a fixed photon energy of $h\nu = 60$ eV, with an instrumental resolution of about 0.6 eV, which mainly depends on the pass energy in the electron analyzer. In the data analysis, the yield of each fragment is determined as a function of the electron binding energy, after the subtraction of the random coincidences. The yield of each m/z fragment has been evaluated by integrating the corresponding time-of-flight region in the PEPICO

Table 1
Appearance Energies (in eV) for Photoions Measured Using PEPICO and TOF Methods

	4H-Pyr					6H-Pyr					16H-Pyr		
Channel	m/z	AE_{PEP}	Err.	AE_{TOF}	Err.	m/z	AE_{PEP}	Err.	AE_{TOF}	Err.	m/z	AE_{PEP}	Err.
M^+	206	7.1	0.1	<13		208	6.9	0.2	<13		218	8.5	0.1
–H	205	12.2	0.1	<13		207	12.3	0.1	<13		217	10.7	0.1
–2H	204	15.1[a]	0.2	<18[a]									
–3H	203	14.5	0.1	14.3	0.3	205	14.4[a]	0.2	16.4[a]	0.2			
–4H	202	16.9[a]	0.1	18.1[a]	0.2								
–5H	201			26.8	0.7								
–6H	200			30.6	0.3								
$-CH_3$	191	12.7	0.1	<13		193	12.7	0.1	<13				
$-CH_4$	190	16.3	0.1	15.9	0.4	192	15.8	0.2	15.3	0.4			
$-CH_5$	189	18.5	0.1	18.5	0.1	191	17.2	0.1	17.5	0.1			
$-CH_6$	188			<24		190			20.0	0.3			
$-CH_7$						189			24.7	0.3			
$-C_2H_2$											192[b]	8.7	0.1
$-C_2H_3$	179	12.1	0.2										
$-C_2H_4$	178	12.4	0.3	<13		180	11.5	0.2	<13		190	11.3	0.1
$-C_2H_5$	177			14.7	0.8	179	13.5	0.1	14.0	0.2	189	11.5	0.1
$-C_2H_6$	176			21.1	0.5	178	16.4	0.1	15.6	0.1			
$-C_2H_7$						177			18.2	0.3			
$-C_3H_5$	165	12.5	0.2	<13							177	11.4	0.1
$-C_3H_6$	164			16.0	1.0	166	13.2	0.1			176	11.4	0.1
$-C_3H_7$	163			26.0	0.6	165	13.0	0.2	<13		175	11.6	0.1
$-C_3H_8$						164			<13				
$-C_4H_7$						153	15.5	0.2					
$-C_4H_8$											162	11.6	0.1
$-C_4H_9$											161	11.4	0.2

Notes.
[a] Significant disagreements between the two methods (due to peak blending in the PEPICO data).
[b] Minor channel, possible impurity.

spectrum over a m/z window of approximately ±0.5 Da. The photofragment yields, when given against the binding energy, represent the breakdown curves. We recorded PEPICO breakdown curves for electron binding energies up to about 24 eV i.e., electron kinetic energies down to about 36 eV. By fitting the first onset of each breakdown curve with two straight lines, the crossing point AE_{PEP} has been extracted and is reported in Table 1. An example of this procedure is given in Figure 3. Due to the steepness of the coincidence breakdown curves and the low statistics close to the onset, the uncertainty from these fits is rather large and the values on AE_{PEP} given in Table 1 should be considered as lower bounds according to the graphical representation of the PEPICO yields. The appearance energy (AE) of a fragment is usually determined by the photoionization efficiency (PIE) measurements, i.e., measuring the ion yield versus photon/electron energy. However, even though the present measurement was performed at a fixed photon energy of 60 eV, the determined values of AE_{PEP} can be considered as a good indication of the fragment's appearance energy.

As a complement to the PEPICO measurements, time-of-flight TOF-MS spectra were recorded over a range of photon energies $h\nu = 13$–32 eV (in steps of 1 eV for $h\nu < 24$ eV, 2 eV for $h\nu > 24$ eV), providing a check of the appearance energy measurements of daughter ions. In the energy range 13–16 eV a certain amount of second-order radiation is present in the incident beam. This contribution has been evaluated and subtracted from the measured mass spectra. Compared with the analysis of the PEPICO spectra, the good statistics in the TOF measurements allowed deconvolution of the isotope distribution in the spectra by fitting each fragment group with a sum of Gaussian functions. Appearance energies AE_{TOF} were determined by a similar procedure as for AE_{PEP}, by fitting a straight line to the TOF branching fraction and taking the zero intercept to be AE_{TOF}. The uncertainties on AE_{TOF} reported in Table 1

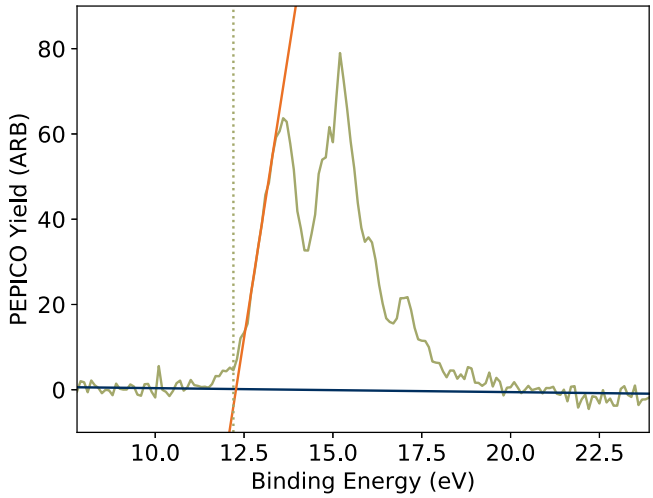

Figure 3. Example of peak edge fitting procedure for determining AE_{PEP}, indicated by the dashed vertical line. Plotted is the PEPICO yield of the $[M\text{-}H]^+$ channel of 4H-Pyr as a function of the electron binding energy.

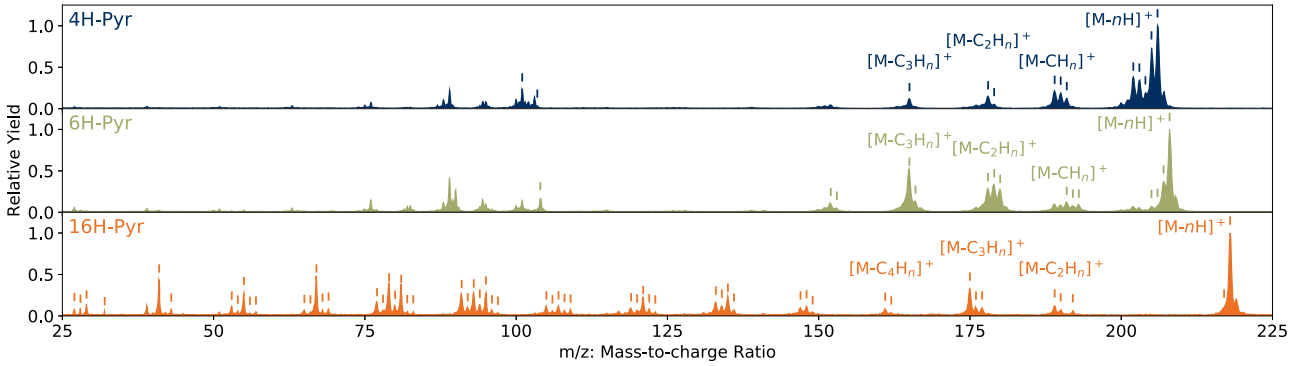

Figure 4. Overview mass spectra of 4H-, 6H-, and 16H-Pyr measured at 60 eV photon energy. The marked peaks are observed in the PEPICO measurement.

reflect only the statistical error in the fit and not the systematic errors related to the large photon energy step size or subtraction of second-order contributions.

The three samples analyzed in this work are all commercially available (TCI Europe). In all cases, a sample size of about 30 mg was inserted in a crucible under vacuum. To minimize possible sample decomposition and contamination of the setup, the samples were kept at the lowest possible temperature to produce a measurable electron signal, i.e., 32 and 39°C, respectively, for 4H- and 6H-Pyr and room temperature for 16H-Pyr. This produced a residual gas pressure in the range of high 10^{-8}–low 10^{-7} mbar, on a base pressure of the vacuum chamber of 1×10^{-8} mbar.

3. Results and Discussion

3.1. Fragmentation Channels

3.1.1. Appearance Energies

Figure 4 shows an overview of TOF mass spectra of the three target molecules following activation by $h\nu = 60$ eV photons. The tick marks above the peaks indicate ions observed in the (separate) PEPICO measurement. The 60 eV TOF spectra of 4H- and 6H-pyrene are qualitatively similar. Multiple peaks corresponding to H-loss channels are observed, as are ions having lost up to 4 C atoms. Doubly charged parent molecules M^{2+} and daughters $[M\text{-}C_mH_n]^{2+}$ are observed close to $m/z \approx 100$. The TOF mass spectrum of 16H-pyrene appears different. The H-loss channels are much less prominent, while significant destruction of the carbon skeleton is observed. Compared to 4H- and 6H-pyrene, many more of the low-mass daughter ions of 16H-Pyr are observed, indicating that they open at comparatively low energy.

Table 1 gives the first onset for the photodissociation of the first several groups of fragments in 4H-, 6H-, and 16H-Pyr, as determined from both the PEPICO measurements (AE_{PEP}) and the TOF mass spectra (AE_{TOF}). For the AE_{TOF} determination, upper limits of $AE_{TOF} < 13$ eV are given in Table 1 for cases where the channel is already open at $h\nu = 13$ eV, the lowest energy measured here. Upper limits are also given in cases where the TOF branching fraction could not be suitably fitted. No determinations of AE_{TOF} are given for 16H-Pyr, where all channels in the table are open at $h\nu = 13$ eV. Note that channels in Table 1 are labeled by the nominal formula of the mass lost from the parent ion, with channels such as CH_5-loss more properly identified as $[M\text{-}CH_{5-x}\text{-}xH]^+$.

In principle, the two methods used for determining AE probe different excitation mechanisms. A PEPICO experiment, which is performed at fixed photon energy, gives photoion yields as a function of the internal energy of the ion. In our TOF measurements, where the yields are measured as a function of the photon energy, contributions are expected from both direct ionization and resonant excitation to bound states of the neutral decaying to the underlying ionization continuum. A comparison of the two measurement schemes is given in Figure 2. For the species considered in this work, resonant excitation is expected to lead to statistical fragmentation. That is, resonant absorption of the full photon energy $h\nu$ is assumed to be converted to internal vibrational energy and redistributed across all internal degrees of freedom before electron emission and dissociation. A significant part of the electron emission is expected to be thermionic (~0 eV electron kinetic energy), leaving the photon energy minus the ionization energy available as internal energy for dissociation. Photofragments formed by this pathway will always appear at lower photon energies than those where significant energy is shared with the departing photoelectron, and will thus dominate the signal at the fragmentation threshold. We thus hypothesize that the PEPICO and TOF measurements should give comparable results.

Generally, the results of the two methods agree within their respective uncertainties. The few exceptions are represented by fragments of weak intensity in the PEPICO spectra, which are adjacent to very intense ones in the region $m/z > 200$, where the peaks are not fully resolved. In these cases, indicated in Table 1, the integration in the time-of-flight region of interest of the PEPICO spectrum includes a contribution from the tail of the neighboring fragments. Here, the AE_{TOF} value, even though affected by a large uncertainty because of the large step in the photon energy, is more reliable as it accounts for the deconvolution of the isotope distribution.

Looking across the table, one sees that the appearance energies for "primary" fragmentation channels (e.g., $[M\text{-}H]^+$ or $[M\text{-}CH_3]^+$) are very similar for 4H- and 6H-Pyr. The values for multistep channels (e.g., $[M\text{-}CH_5]^+$, i.e., $[M\text{-}CH_3\text{-}2H]^+$) are somewhat lower for 6H-Pyr than 4H-Pyr, by about 1 eV on average. On the other hand, the appearance energies for daughter ions of the same mass-to-charge ratio (e.g., $m/z = 205$ or 191) are mostly higher for 6H-Pyr, by more than 2 eV on average. 16H-Pyr has lower appearance energies for all channels.

The values in Table 1 are affected by kinetic shifts (Lifshitz 2002). Kinetic shifts are a consequence of the rapidly increasing dissociation rate constant above threshold and the short sampling time between activation of the molecules and extraction of the photoions by the mass spectrometer, estimated

Table 2
Calculated Dissociation Energies (B3LYP/6-31G(d), in eV) for Important Fragmentation Channels

Channel	4H-Pyr	6H-Pyr	16H-Pyr
–H	2.4	2.6	2.0
–2H	4.9	5.2	5.1
$-CH_3$	2.2	2.3	1.6
$-C_2H_4$	1.3/6.1	3.9	2.4
$-C_3H_6$	⋯	6.2	2.2

Note. Values for 6H- and 16H-Pyr from Gatchell et al. (2015). For C_2H_4-loss from 4H-Pyr, two values are given; the smaller is for direct cleavage and the larger includes rearrangement of the remaining two additional H atoms.

to be ≈0.5 μs for our instrument. Simply put, the lifetime of the decaying molecules is short compared to the observation time. This effect is most severe for activation energies just above the dissociation threshold, leading to a shift in the measured appearance energy. In our experiments, we expect kinetic shifts to be of similar magnitude for analogous fragmentation channels. For a given dissociation energy, the kinetic shift should increase with the number of degrees of freedom over which the internal energy is distributed. Thus the measured AE should increase with the degree of hydrogenation, contrary to some of the trends identified here.

3.1.2. Dissociation Energies

Dissociation energies have been calculated for 4H-Pyr by using the density functional theory at the B3LYP/6-31G(d) level of theory using GAUSSIAN09 (Frisch et al. 2009). The calculated dissociation energies are given in Table 2, and the structures of the parent and product ions are illustrated in the Appendix. Corresponding values for 6H- and 16H-Pyr are taken from Gatchell et al. (2015), who used the same computational approach. Dissociation energies account only for the difference in energy between the initial and final states, and do not consider energy barriers or transition states or kinetic shifts. Thus, the dissociation energies (Table 2) are not directly comparable to the appearance energies (Table 1), and we limit our discussion here to general trends and gross discrepancies in the data.

For 4H- and 6H-Pyr, the experimental appearance energies for H- and CH_3-loss (Table 1) lie about 5 eV above the ionization threshold, or equivalently 2–3 eV above the dissociation energy (Table 2). This excess energy—which is much larger than the energy barriers to H-loss (Cazaux et al. 2016) or H-migration (Castellanos et al. 2018b)—is attributed to a kinetic shift (Lifshitz 2002). The kinetic shift for 4H- and 6H-Pyr is comparable to, though somewhat less than that measured for pristine pyrene (Ling et al. 1995), although precise comparisons cannot be made between shifts measured with different instruments. In contrast, despite the larger number of vibrational degrees of freedom over which the excitation is distributed, the kinetic shift for 16H-Pyr is small, implying much higher dissociation rate constants. The similarity of the dissociation energies for H-loss and backbone fragmentation underscores the importance of the competition between these pathways to the photostability of HPAHs.

According to our calculations, the energy required to liberate a hydrogen atom is about 2.5 eV, in agreement with calculations for superhydrogenated coronene (Cazaux et al. 2016), although higher than for some smaller HPAHs

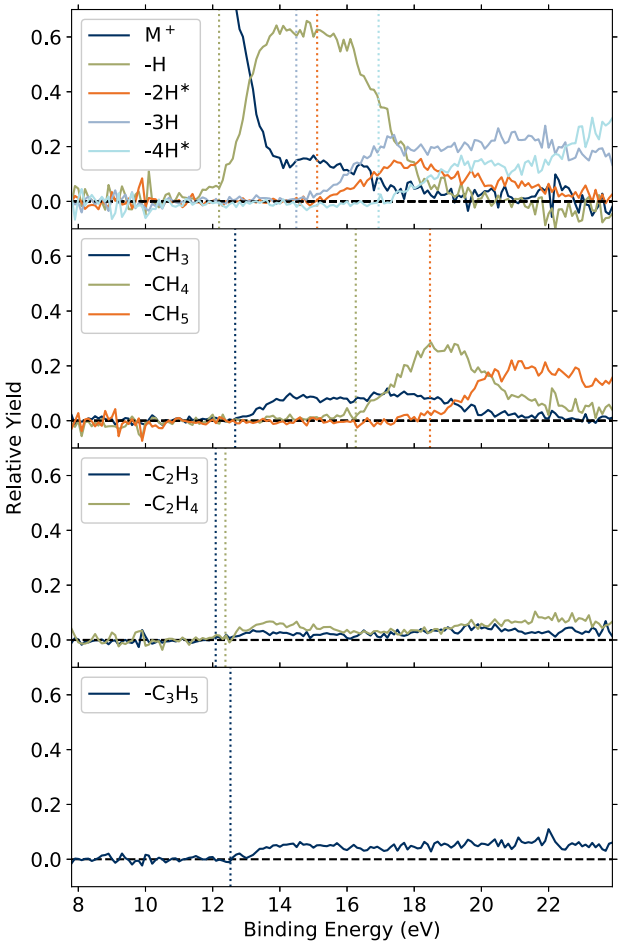

Figure 5. PEPICO yields for nH- and C_mH_n-loss from 4H-Pyr. Vertical dotted lines indicate AE_{PEP}. See the discussion of possible peak blending in Section 3.1.1.

(Diedhiou et al. 2020). This value is also consistent with the experimental finding that the appearance energy for the $m/z = 201$, 200 daughter ions from 4H-Pyr are shifted by about 10 eV, 2.5 eV per additional H, relative to pristine pyrene (Ling et al. 1995; Jochims et al. 1999; West et al. 2014c; Rouillé et al. 2015).

3.2. Branching Fractions

3.2.1. 4H-Pyr

Figure 5 shows the relative PEPICO yields for the main fragmentation channels of 4H-Pyr. Several fragmentation channels open at similar binding energies around 12.4 eV. The loss of a single H atom is the channel with by far the highest branching fraction. Backbone fragmentation channels, most importantly CH_3- and C_2H_4-loss, are also observed. In Table 2, two values for the C_2H_4-loss dissociation energy are given. The higher value (6.1 eV) corresponds to direct cleavage while the lower (1.3 eV) includes the stabilizing effect of the remaining two excess H atoms saturating the dangling bonds at the cleavage site, giving the phenanthrene cation as the final product. The structures of these two product ions are shown in Figure 6. Given that the relative yield of C_2H_4-loss is rather low, the complex rearrangement required for the low-energy pathway may be kinetically disfavored (recall that the dissociation energies do not include barriers). On the other

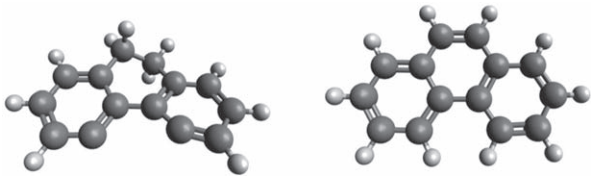

Figure 6. Proposed structures of product ions formed by C_2H_4-loss from 4H-Pyr. Left: result of direct cleavage of a C_2H_4 group with dissociation energy 6.1 eV. Right: result after rearrangement of H atoms yielding phenanthrene cation with dissociation energy 1.3 eV.

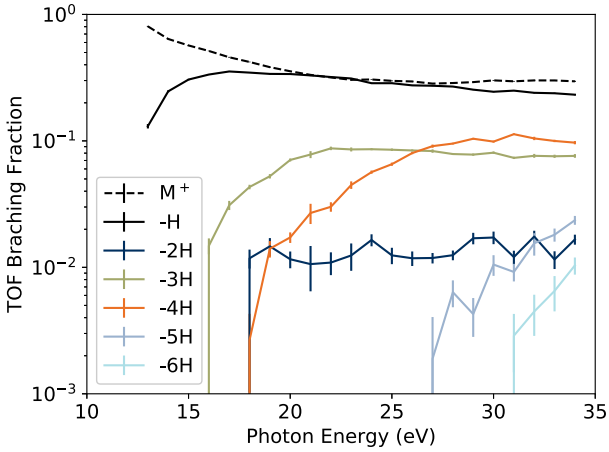

Figure 7. Relative TOF yields for nH-loss from 4H-Pyr.

hand, other minor channels opening at the same binding energy are C_2H_3- and C_3H_5-loss, which have calculated dissociation energies of 3.4 and 2.3 eV, respectively. These channels do not correspond to any simple bond cleavage and suggest that H-migration is an important step in the fragmentation process (Solano & Mayer 2015).

At higher binding energies, a sequence of further hydrogen losses emerges, as do additional backbone fragmentation channels. The CH_4- and CH_5-loss channels appear at energies where the $[M\text{-}H]^+$ and $[M\text{-}2H]^+$ yields are decreasing, leading to the interpretation that the former ions are formed through CH_3-loss from the latter i.e., $M^+ \rightarrow [M\text{-}H]^+ + H \rightarrow [M\text{-}CH_4]^+ + H + CH_3$. In contrast, the $[M\text{-}3H]^+$ and $[M\text{-}4H]^+$ ions, which correspond to the protonated and radical pyrene cation, are present up to at least 24 eV.

Although not seen in the PEPICO data, the $[M\text{-}5H]^+$ and $[M\text{-}6H]^+$ daughter ions are observed in our energy-dependent TOF mass spectra (which extend to higher energy), shown in Figure 7. These channels, appearing at $h\nu = 26.8$ and 30.6 eV, respectively, correspond to the loss of native H atoms. The previously reported appearance energies for these same daughter ions starting from pristine pyrene are 16.3 eV (Ling et al. 1995; Jochims et al. 1999; Rouillé et al. 2015) and 19.2 eV (Ling et al. 1995). The four additional H atoms on 4H-Pyr thus provide a buffering capacity against the loss of native hydrogens on the order of 10 eV. This is an intuitive quantification of the protective effect first reported for superhydrogenated coronene cations (Reitsma et al. 2014). We stress, however, that in the case of 4H-Pyr there are several open backbone fragmentation pathways that compete with dehydrogenation.

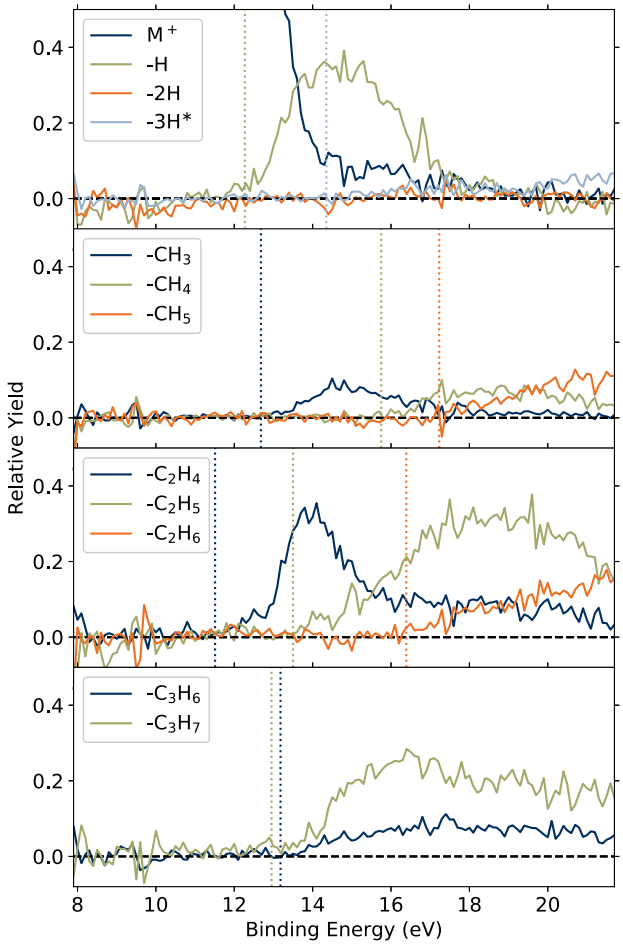

Figure 8. PEPICO yields for nH- and C_mH_n-loss from 6H-Pyr. Vertical dotted lines indicate AE_{PEP}. See the discussion of possible peak blending in Section 3.1.1

3.2.2. 6H-Pyr

Figure 8 shows the relative PEPICO yields for the main fragmentation channels of 6H-Pyr. As for 4H-Pyr, several fragmentation channels open around 12.4 eV. In contrast, however, the branching fractions for H- and C_mH_n-loss for 6H-Pyr are nearly equal. Further dehydrogenation leading to pristine pyrene is not significant. The protective effect of superhydrogenation is not as important for this molecule, in agreement with previous studies using other means of activation (Gatchell et al. 2015; Wolf et al. 2016a, 2016b).

The nominal C_3H_7-loss channel is surprisingly strong. This channel likely results from cascade processes that involve either C_2H_4- and CH_3-loss or C_3H_6- and H-loss.

3.2.3. 16H-Pyr

Figure 9 shows the relative PEPICO yields for the first several fragment groups of 16H-Pyr. Compared to 4H- and 6H-Pyr, H-loss is a minor channel for 16H-Pyr, with backbone fragmentation dominating. Several backbone fragmentation channels and H-loss open at binding energies around 11.5 eV, only about 3 eV above the ionization threshold.

Interestingly, CH_3-loss is not detected, despite this being the channel with the lowest calculated dissociation energy (Gatchell et al. 2015). It may be that $[M\text{-}CH_3]^+$ daughter ions are formed but with sufficient internal energy to further

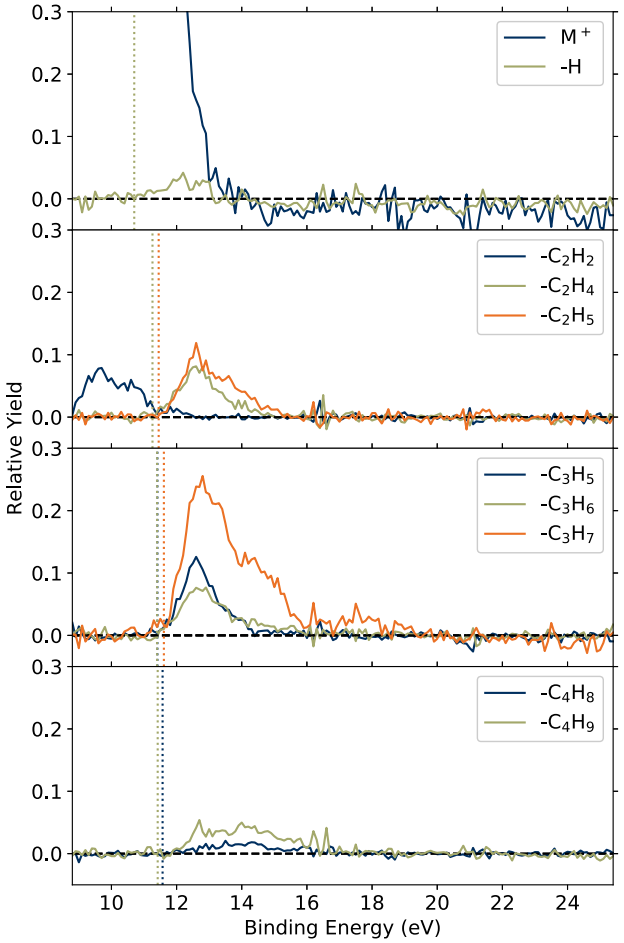

Figure 9. PEPICO yields for H- and C_mH_n-loss from 16H-Pyr. Vertical dotted lines indicate AE_{PEP}. Note that there are several additional fragmentation channels open in this energy range (see Figure 4) that are not plotted. The total relative yield of the channels shown here is thus less than unity.

fragment. Much like for 6H-Pyr, this could explain the prominence of channels such as C_3H_7-loss ($[M\text{-}CH_3\text{-}C_2H_4]^+$) and C_4H_9-loss ($[M\text{-}CH_3\text{-}C_3H_6]^+$), although these could also correspond to $[M\text{-}H\text{-}C_3H_6]^+$ and $[M\text{-}H\text{-}C_4H_8]^+$.

Just beyond the ionization threshold for 16H-Pyr, a product with $m/z = 192$ is observed, labeled as C_2H_2-loss in Figure 9. This is not an energetically favored dissociation channel, and the very low activation energy suggests that dissociation occurs along an excited state pathway before internal conversion. However, in the present experiment, we are unable to exclude the possibility of a sample impurity such as possibly tetradecahydro-anthracene.

Regardless of the details of the fragmentation pathways, it is clear that in the extreme case of fully saturated 16H-Pyr, the weakening effect of replacing aromatic bonds with aliphatic ones is much more important than the buffering effect of the additional hydrogen atoms.

3.2.4. Summary

By way of summary, Figure 10 shows the branching fractions of the first few fragment groups from the PEPICO measurement at a common electron binding energy of 13.6 eV. This energy corresponds to the highest photon energy expected to impinge on HPAHs in PDRs (Montillaud et al. 2013; Boschman et al. 2015). At this energy, the majority of

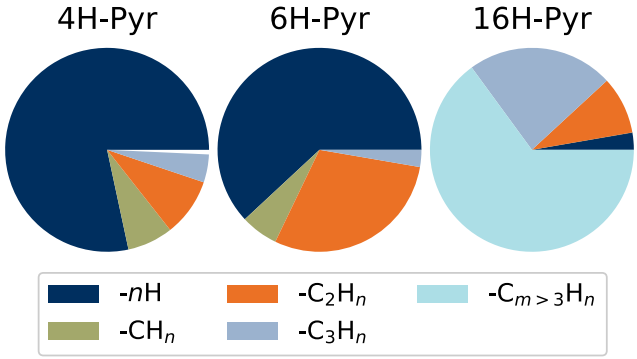

Figure 10. Comparison of the branching fractions of the first few fragment groups at a binding energy of 13.6 eV.

photoactivated 4H- and 6H-Pyr ions remain intact or have suffered only H-loss. The backbone fragmentation fraction of 6H-Pyr is more than 15% higher than that of 4H-Pyr. However, only a tiny fraction of 16H-Pyr photoions remain intact, with most losing more than three C atoms. A similar trend is observed for the smaller catacondensed PAHs anthracene and phenanthrene, where H- and CH_3-loss are dominant for the di-hydrogenated species (West et al. 2014a; Diedhiou et al. 2020), but larger carbon-containing fragments become more important with increasing hydrogenation (Diedhiou et al. 2020). The branching fractions in Figure 10 can be compared to pristine pyrene, where 100% of photoions remain intact at 13.6 eV binding energy (Ling et al. 1995; Jochims et al. 1999; Rouillé et al. 2015). Overall, the trend is consistent with decreasing stability of the carbon backbone with an increasing degree of superhydrogenation.

4. Implications for Astrophysics

Multiple closely related H_2-formation mechanisms involving PAHs have been proposed to explain the high observed H_2 abundance in PDRs (Bauschlicher 1998; Hirama et al. 2004; Mennella et al. 2012; Chen et al. 2015; Castellanos et al. 2018a; Ferullo et al. 2019). Here we consider a cycle where H atoms are gradually added to a PAH, with sufficient time between additions for the molecule to relax to its global minimum energy structure and radiate away any excess internal excitation. H_2-emission is finally induced by the absorption of a UV photon.

For a truly catalytic cycle for H_2-formation involving PAHs, the carbon backbone must be preserved with near-unit probability. We have shown that this criterion is not met for superhydrogenated pyrene. Figure 11 presents a simple model for the survival probabilities upon repeated excitation assuming that the outcome follows the probability mass function of the binomial distribution. Taking the C_mH_n-loss branching fractions ($m \geqslant 1$) from the previous section as destruction probabilities in competition with H_2 evolution, one finds even in the best case (4H-Pyr) that 90% of the "catalyst" is depleted after only 10 cycles, as illustrated in Figure 11. To complete a successful catalytic cycle, at least two added H atoms are required while leaving the underlying PAH intact. Extrapolating the trend in survival probability for 6H- and 4H-Pyr down to 2H-Pyr, one may hypothesize that this minimal catalytic unit could last up to 40 cycles before 90% depletion. Note that our simple model makes the unrealistic assumption that surviving ions always return to their original hydrogenation level before

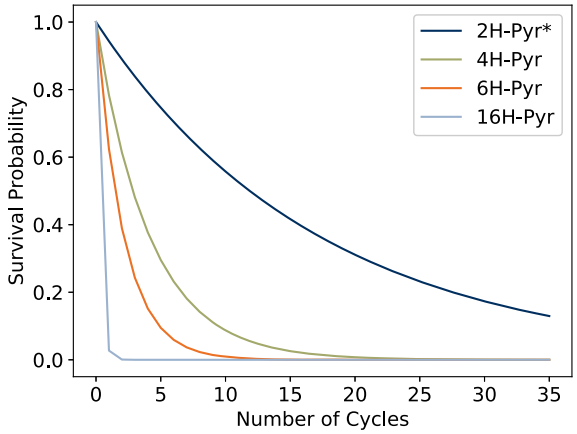

Figure 11. Depletion of HPAH "catalysts" following sequential hydrogenation-excitation-fragmentation cycles. The backbone fragmentation branching fractions (Figure 10) are taken as survival probabilities. The survival probability of 2H-Pyr is extrapolated from the trend from 4H- to 6H-Pyr.

the next excitation event, and the curves in Figure 11 should be viewed as average values for typical hydrogenation levels.

The stability trend of HPAHs depends on size. For the pyrene family, H-loss and backbone fragmentation have roughly equal branching fractions near threshold at a superhydrogenation level $N = 6$ (Figure 8). For the smaller catacondensed PAHs anthracene and phenanthrene, the crossover occurs already between $N = 2$ and 4 additional H atoms (Diedhiou et al. 2020). An infrared multiphoton dissociation study of superhydrogenated coronene found the branching fractions to be comparable at $N = 7$ (Cazaux et al. 2019). For coronene and the larger PAHs expected to be predominant in PDRs, it may be expected—though this has not been demonstrated—that hydrogenated species with the minimal amount of superhydrogenation to achieve catalytic H_2 formation could approach 100% stability against loss of native H atoms and backbone fragmentation. However, as sequential hydrogenation past the first added H atom faces greatly reduced or vanishing energy barriers (Rauls & Hornekær 2008), this would require fine balancing between the rates of H-addition and photoexcitation leading to H_2 evolution. In a PDR, there may thus exist a thin layer in which these processes are balanced and catalytic activity of coronene is viable. Larger PAHs with wider windows of stability upon hydrogenation could be active over correspondingly thicker layers in the PDR.

The structures of the molecules in our model system (Figure 1) are highly symmetric. Studies of superhydrogenated coronene have found that sequential hydrogenation produces highly asymmetric structures due to the fact that attachment of a hydrogen atom structurally changes the PAH locally, facilitating the attachment of more H atoms in the vicinity (Cazaux et al. 2016, 2019). Asymmetric hydrogenation may lead to highly hydrogenated domains with locally weaker carbon backbones compared to a symmetrically hydrogenated PAH at the same hydrogenation level. However, it may also be that, given the lower H atom fluxes in PDRs compared to the experiments, asymmetrically hydrogenated HPAHs could have time to relax to lower energy symmetric structures (Pla et al. 2020).

5. Conclusions

We have presented a study of the stability of a series of super-hydrogenated pyrene molecules against fragmentation by VUV photons. Using the PEPICO method, we have determined the formation energetics and branching fractions for the most significant H-loss and carbon backbone fragmentation channels. In each case, we find that H- and C_mH_n-loss channels open at similar energies. We observe a clear trend in the branching fractions, which increasingly favor backbone fragmentation with increasing hydrogenation. Similar trends have been recently reported for smaller, catacondensed HPAHs (Diedhiou et al. 2020). We conclude that pyrene is too small to act as a true catalyst for H_2 formation in PDRs.

We find that, compared to pristine Pyr ($C_{16}H_{10}$), the internal energies required to form daughter ions that have lost the first native hydrogens ($C_{16}H_9^+$ and $C_{16}H_8^+$) are about 10 eV higher for 4H-Pyr ($C_{16}H_{14}$), or 2.5 eV per H atom. This corresponds to the typical binding energies of H atoms to PAH cations (Cazaux et al. 2016). We also observe that the lowest fragmentation energies are about 2 eV higher for 6H-Pyr than for 4H-Pyr, or 1 eV per H atom.

The increasing probability of PAH backbone fragmentation, and the corresponding decrease in catalytic potential, with increasing degrees of superhydrogenation is an important effect to consider in astrochemical models. More laboratory work is needed, particularly on "edge" cases like small pericondensed PAHs, to support such modeling efforts with quantitative branching fractions and their trends with PAH size and structure.

This work was supported by the Swedish Research Council (grant Nos. 2016–03675, 2016–04181), the Carl Trygger Foundation (grant No. 17:436), the Swedish Foundation for International Collaboration in Research and Higher Education (STINT, grant No. PT2017-7328 awarded to J.N.B., E.C., and M.H.S.), and the MAECI-VR Italy–Sweden project "Novel molecular tools for the exploration of the nanoworld" (VR grant No. 2018–00913). This article is based upon work from COST Action CA18212—Molecular Dynamics in the GAS phase (MD-GAS), supported by COST (European Cooperation in Science and Technology).

Appendix
Calculated Structures

Figures A1–A5 show the optimized structures of the parent and daughter ions used in calculating the dissociation energies in Table 2.

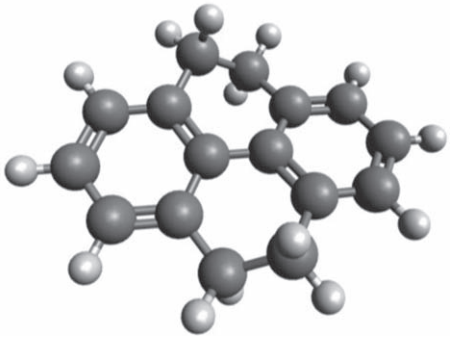

Figure A1. Structure of parent ion 4H-Pyr, i.e., M^+.

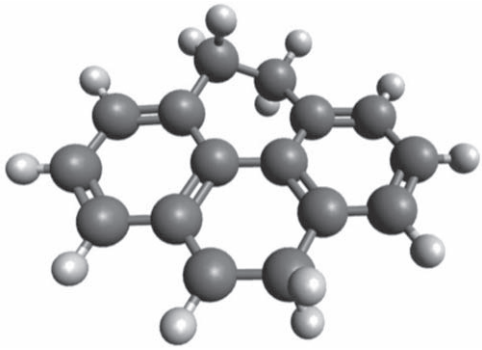

Figure A2. Structure of product ion of H-loss from 4H-Pyr, i.e., $[M\text{-}H]^+$.

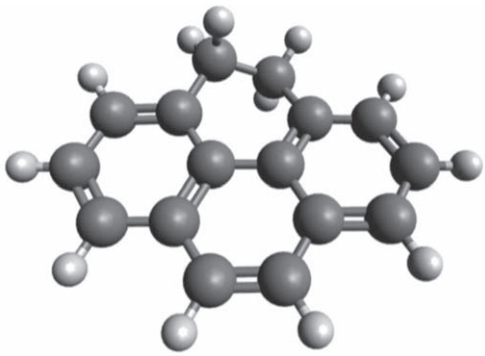

Figure A3. Structure of product ion of 2H-loss from 4H-Pyr, i.e., $[M\text{-}2H]^+$.

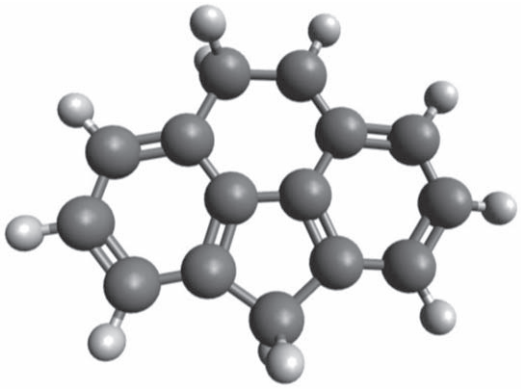

Figure A4. Structure of product ion of CH_3-loss from 4H-Pyr, i.e., $[M\text{-}CH_3]^+$.

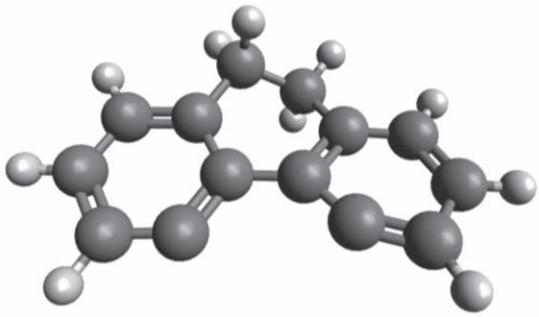

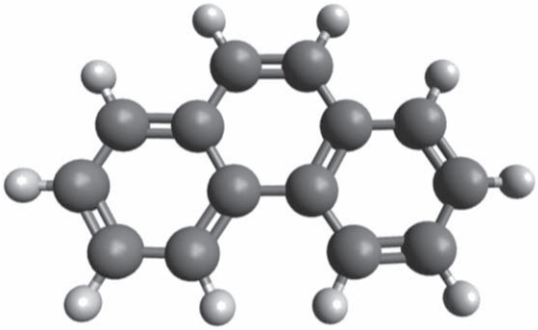

Figure A5. Structures of product ions of C_2H_4-loss from 4H-Pyr, i.e., $[M\text{-}C_2H_4]^+$. The upper structure is the result of direct cleavage of a C_2H_4 group while the bottom shows the global minimum energy structure, which requires rearrangement of H atoms.

References

Allamandola, L. J., Tielens, A. G. G. M., & Barker, J. R. 1989, ApJS, 71, 733
Bauschlicher, C. W., Jr. 1998, ApJL, 509, L125
Boschman, L., Cazaux, S., Spaans, M., Hoekstra, R., & Schlathölter, T. 2015, A&A, 579, A72
Boschman, L., Reitsma, G., Cazaux, S., et al. 2012, ApJL, 761, L33
Castellanos, P., Candian, A., Andrews, H., & Tielens, A. 2018a, A&A, 616, A167
Castellanos, P., Candian, A., Zhen, J., Linnartz, H., & Tielens, A. 2018b, A&A, 616, A166
Cautero, G., Sergo, R., Stebel, L., et al. 2008, NIMPA, 595, 447
Cazaux, S., Arribard, Y., Egorov, D., et al. 2019, ApJ, 875, 27
Cazaux, S., Boschman, L., Rougeau, N., et al. 2016, NatSR, 6, 19835
Chen, T., Gatchell, M., Stockett, M. H., et al. 2015, JChPh, 142, 144305
Chiarinelli, J., Bolognesi, P., Domaracka, A., et al. 2018, PCCP, 20, 22841
Cruz-Diaz, G. A., Ricca, A., & Mattioda, A. L. 2020, ESC, 4, 1730
Derossi, A., Lama, F., Piacentini, M., Prosperi, T., & Zema, N. 1995, RScI, 66, 1718
Diedhiou, M., West, B. J., Bouwman, J., & Mayer, P. M. 2019, JPCA, 123, 10885
Diedhiou, M., West, B. J., & Mayer, P. M. 2020, MolAs, 19, 100071
Ferullo, R. M., Zubieta, C. E., & Belelli, P. G. 2019, PCCP, 21, 12012
Foley, N., Cazaux, S., Egorov, D., et al. 2018, MNRAS, 479, 649
Frisch, M. J., Trucks, G. W., Schlegel, H. B., et al. 2009, Gaussian 09 Revision A.01 (Wallingford, CT: Gaussian, Inc)
Fu, Y., Szczepanski, J., & Polfer, N. C. 2011, ApJ, 744, 61
Gatchell, M., Stockett, M. H., de Ruette, N., et al. 2015, PhRvA, 92, 050702(R)
Habart, E., Boulanger, F., Verstraete, L., et al. 2003, A&A, 397, 623
Habart, E., Boulanger, F., Verstraete, L., Walmsley, C., & Des Forêts, G. P. 2004, A&A, 414, 531
Hirama, M., Tokosumi, T., Ishida, T., & Aihara, J.-i. 2004, ChPhy, 305, 307
Hollenbach, D., & Salpeter, E. E. 1971, ApJ, 163, 155
Jochims, H. W., Baumgrtel, H., & Leach, S. 1999, ApJ, 512, 500
Klærke, B., Toker, Y., Rahbek, D. B., Hornekær, L., & Andersen, L. H. 2013, A&A, 549, A84
Lifshitz, C. 2002, Eur. J. Mass Spectrom., 8, 85
Ling, Y., Gotkis, Y., & Lifshitz, C. 1995, Eur. J. Mass Spectrom., 1, 41
Mackie, C. J., Candian, A., Huang, X., et al. 2018, PCCP, 20, 1189

Mayer, P. M., Blanchet, V., & Joblin, C. 2011, JChPh, 134, 244312
Menk, R. H., Antonelli, M., Brajnik, G., et al. 2019, in AIP Conf. Proc. 2054 (Melville, NY: AIP), 060071
Mennella, V., Hornekær, L., Thrower, J., & Accolla, M. 2012, ApJL, 745, L2
Micelotta, E. R., Jones, A. P., & Tielens, A. G. G. M. 2010, A&A, 510, A36
Mishra, P. M., Avaldi, L., Bolognesi, P., et al. 2014, JPCA, 118, 3128
Montillaud, J., Joblin, C., & Toublanc, D. 2013, A&A, 552, A15
Pauzat, F., & Ellinger, Y. 2001, MNRAS, 324, 355
Pla, P., Wang, Y., Martín, F., & Alcamí, M. 2020, PCCP, 22, 21968
Plekan, O., Coreno, M., Feyer, V., et al. 2008, PhyS, 78, 058105
Postma, J., Bari, S., Hoekstra, R., Tielens, A. G. G. M., & Schlathölter, T. 2010, ApJ, 708, 435
Rapacioli, M., Cazaux, S., Foley, N., et al. 2018, PCCP, 20, 22427
Rauls, E., & Hornekær, L. 2008, ApJ, 679, 531
Reitsma, G., Boschman, L., Deuzeman, M. J., et al. 2014, PhRvL, 113, 53002
Rouillé, G., Krasnokutski, S. A., Fulvio, D., et al. 2015, ApJ, 810, 114
Sandford, S. A., Bernstein, M. P., & Materese, C. K. 2013, ApJS, 205, 8
Schlathölter, T., Mostafa, Y., Kamman, A., et al. 2020, EPJD, 74, 114
Solano, E. A., & Mayer, P. M. 2015, JChPh, 143, 104305
Stockett, M. H., Gatchell, M., Chen, T., et al. 2015, J. Phys. Chem. Lett., 6, 4504
Szczepanski, J., Oomens, J., Steill, J. D., & Vala, M. T. 2010, ApJ, 727, 12
Thrower, J. D., Friis, E. E., Skov, A. L., Jørgensen, B., & Hornekær, L. 2014, PCCP, 16, 3381
Thrower, J. D., Jørgensen, B., Friis, E. E., et al. 2012, ApJ, 752, 3
Tielens, A. G. G. M. 2005, The Physics and Chemistry of the Interstellar Medium (Cambridge: Cambridge Univ. Press)
Tielens, A. G. G. M. 2008, ARA&A, 46, 289
Vala, M., Szczepanski, J., Oomens, J., & Steill, J. D. 2009, JAChS, 131, 5784
Wagner, D. R., Kim, H., & Saykally, R. J. 2000, ApJ, 545, 854
West, B., Joblin, C., Blanchet, V., et al. 2014a, JPCA, 118, 1807
West, B., Lowe, B., & Mayer, P. M. 2018, JPCA, 122, 4730
West, B., Sit, A., Mohamed, S., et al. 2014b, JPCA, 118, 9870
West, B., Useli-Bacchitta, F., Sabbah, H., et al. 2014c, JPCA, 118, 7824
Wolf, M., Giacomozzi, L., Gatchell, M., et al. 2016a, EPJD, 70, 1
Wolf, M., Kiefer, H. V., Langeland, J., et al. 2016b, ApJ, 832, 24